LASER INTERFEROMETER GRAVITATIONAL WAVE OBSERVATORY
- LIGO -
CALIFORNIA INSTITUTE OF TECHNOLOGY
MASSACHUSETTS INSTITUTE OF TECHNOLOGY

| Technical Note | LIGO-T2400197–v1 | 2024/08/06 |
|---|---|---|

# Improving the Robustness of Next-Generation Wavefront Control: Characterization and Analysis of FROSTI Heating Profiles

Xuejun A. Fu

**California Institute of Technology**
**LIGO Project, MS 18-34**
**Pasadena, CA 91125**
Phone (626) 395-2129
Fax (626) 304-9834
E-mail: info@ligo.caltech.edu

**Massachusetts Institute of Technology**
**LIGO Project, Room NW22-295**
**Cambridge, MA 02139**
Phone (617) 253-4824
Fax (617) 253-7014
E-mail: info@ligo.mit.edu

**LIGO Hanford Observatory**
**Route 10, Mile Marker 2**
**Richland, WA 99352**
Phone (509) 372-8106
Fax (509) 372-8137
E-mail: info@ligo.caltech.edu

**LIGO Livingston Observatory**
**19100 LIGO Lane**
**Livingston, LA 70754**
Phone (225) 686-3100
Fax (225) 686-7189
E-mail: info@ligo.caltech.edu

http://www.ligo.caltech.edu/

# 1 Introduction

The prediction of gravitational radiation as an outcome of Einstein's General Theory of Relativity resulted in a new pursuit of observational evidence for what was originally a highly debated phenomenon. Whilst the discovery of pulsars validated the existence of gravitational waves (GWs) through measurements of energy loss that would have been caused by gravitational radiation emission, gravitational waves themselves evaded detection [1]. In order to detect GWs, large ground-based interferometers were required. The first generation of detectors included TAMA located near Tokyo, Japan; GEO located near Hannover, Germany; Virgo located near Pisa, Italy; and the two LIGO facilities (dubbed initial LIGO or iLIGO to separate it from the later advanced LIGO or aLIGO) located in Livingston, LA and Hanford, WA [1]. Together, they formed a global network of gravitational wave detectors. For the purposes of this topic, the primary focus will be on LIGO. The initial construction of the LIGO detector was not expected to yield direct detection of gravitational waves, but rather place a range on LIGO's sensitivity and provide information on the limitations of the instruments [2]. An overhaul of much of the hardware would eventually lead to greater success in the performance of Advanced LIGO showcased by its first detection of gravitational waves in 2015 [1,2].

## 1.1 Gravitational Waves

Gravitational waves can be described as perturbations through spacetime known as a strain in spacetime represented by

$$\mathrm{h}_{\mu\nu}(z,t) = \begin{pmatrix} 0 & 0 & 0 & 0 \\ 0 & -h_+ & h_\times & 0 \\ 0 & h_\times & h_+ & 0 \\ 0 & 0 & 0 & 0 \end{pmatrix} \qquad (1)$$

where $\mathrm{h}_+$ and $\mathrm{h}_\times$ are amplitudes for the two polarization of the wave [1].

Sources of GWs typically include pulsars, compact binary object mergers (inspiral of neutron stars and black holes), and cosmic background radiation, though detected GWs have currently only been from compact binary object inspirals and mergers [1]. The need for gravitational radiation in the Theory of Relativity stems from the need for gravity to be causal, that is, changes in gravitational exertions must be communicated to a distant observer somehow. Just as electromagnetic waves come from accelerated charges, gravitational waves come from accelerated masses [3]. Due to the high rigidity of spacetime, these masses must be extremely large and moving at relativistic speeds in order for gravitational waves to be detectable [1]. As a result, production of GWs in a laboratory is unattainable and requires turning toward astrophysical objects instead. Thus, large detectors are needed. By pushing the limits of gravitational wave detectors, a new tool for studying astronomical phenomena and features arises such as bypassing the obstruction of light from the early universe by analyzing primordial gravitational waves.

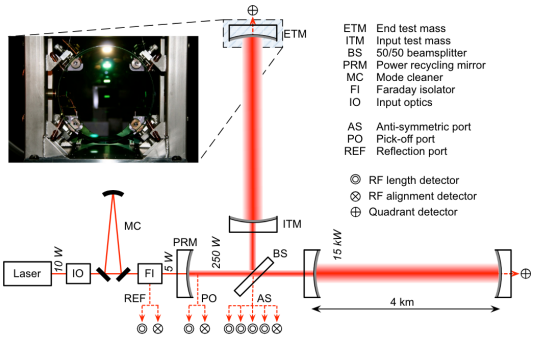


Figure 1: Diagram of the current aLIGO layout originally from Ref. [4].

## 1.2 LIGO Interferometer

The LIGO interferometers utilize a similar layout to a Michelson interferometer on a much larger scale and within a vacuum system. The facilities consist of two equidistant arms, 4-km in length, that are orthogonally oriented with

each other [1]. At the ends of each arm rests a suspended high reflectivity mirror which are referred to as "test masses," as they are meant to be free from forces and be able to follow the distortions of spacetime [2]. At the intersection of the two arms is a laser beam splitter that evenly splits the incoming beam into two sending one to each arm before reflecting and recombining. The resultant beam is sent to a photodetector that reads the signal. As the arm lengths are made equidistant, the beams travel the same distance and form an interference pattern upon recombining. However, when a gravitational wave passes by, the arm lengths are distorted and a phase shift occurs affecting the resultant interference and altering the measured power.

#### 1.2.1 Fabry-Perot Cavities

Gravitational waves are extremely difficult to detect, therefore, increasing the sensitivity of the interferometer is needed. This can be done by utilizing Fabry-Perot, Power Recycling, and Signal Recycling Cavities. Despite having 4-km length arms for the laser light to travel through, greater lengths are needed to better detect GWs. Financial and physical limitations prevent the arms from being any longer, but luckily, the use of Fabry-Perot cavities artificially increases the distance photons must travel within the arms. By placing a mirror by the beam splitter and 4-km away from the end test mass in each arm, the photons bounce between the two mirrors about 300 times in the same spot before exiting the cavity [1]. This increases the travel distance from 4-km to roughly 1200-km [2]. This also means any distortions to the arms will change the distance traveled by a greater amount, thereby increasing the phase shift caused by GWs [1].

#### 1.2.2 Power Recycling

The power of the laser is also a hindrance to the viability of the interferometer. A laser power close to 750kW is needed to allow detection of GWs which is impractical to build [2]. To resolve this issue, power recycling is used to increase a 40W input laser to operate on a 750kW scale. To ensure most of the light returns to the laser, the arm lengths are fine-tuned microscopically to interfere destructively at the photodetector [1]. A mirror can then be placed just before the beam splitter which would allow the input laser to pass through but reflect the return beam back into the interferometer to interfere constructively [1]. This recycling of the laser increases the stored power in the Fabry-Perot cavities, increasing the amount of photons within the cavities.

#### 1.2.3 Signal Extraction

Using the same concepts as power recycling to amplify the power, signal amplification can be done through the Signal Recycling Cavity (SRC). The SRC operates in two modes: signal recycling and Resonant Sideband Extraction (RSE). The signal recycling mode ensures the (carrier) laser field is resonant resulting in a narrow detector bandwidth. On the other hand, adjusting the cavity length for RSE causes the carrier field to be anti-resonant. aLIGO operates under RSE to allow for minimal thermal distortions on the mirrors that would otherwise occur with storing high amounts of power in the cavities while not limiting the frequency of GWs that could be amplified [1]. It then becomes possible to tune the frequency response for GW signals with careful placement of the signal recycling mirror between the beam splitter and photodetector [5]. For the future Cosmic Explorer, the SRC will be renamed to the Signal Extraction Cavity.

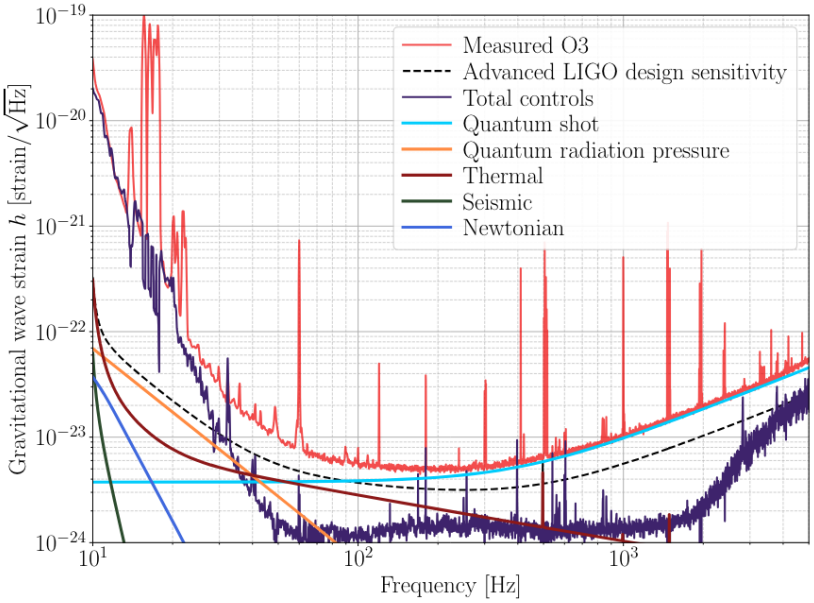


Figure 2: Noise budget of O3 LIGO Hanford, originally from Ref. [6].

### 1.3 Noise Sources

Despite the increasing sensitivity of the interferometer, noise sources still pose an issue. Seismic Noise, Newtonian Gravity Noise, Controls Noise, Quantum Noise, and Thermal Noise all create displacement noise by producing motion on the test masses [1]. As a result of having power in the low frequency range, these effects then affect the detection of low frequency astrophysical sources and must be minimized accordingly [1]. Much of the development on the current aLIGO focuses on the reduction of noise within the interferometer.

#### 1.3.1 Seismic Noise

To combat seismic vibrations that naturally occur in the Earth, two systems are employed known as Passive Vibration Reduction (PVR) and Active Vibration Reduction (AVR). PVR utilizes the properties of pendulums and the law of inertia to suspend the test masses in a state of "free fall". By constructing "quad" suspensions for the test masses, they are able to absorb vibrations not canceled out by the AVR system and keep the test mass steady [2]. The AVR system utilizes seismometers around the observatory to detect any major seismic motions caused by earthquakes, traffic, or tidal gravity from the moon and sun [1]. A signal is then sent to a feedback system which can determine a countermotion for the isolation system around the quads to cancel out terrestrial vibrations before they can reach the test masses [2].

#### 1.3.2 Newtonian Gravity Noise

Compared to seismic noise, Newtonian Gravity noise is much more difficult to filter out. It originates from perturbations in the local gravitational field due to atmospheric density fluctuations and surface waves [1]. Due to its nature, there is no way to physically shield the test masses from this type of noise with the current LIGO scheme (unlike detectors with underground infrastructures could such as KAGRA or the Einstein Telescope [1]) so the best approach would be to implement active noise cancellation through adaptive noise canceling algorithms [7]. This focus of study will become much more prevalent with third-generation GW detectors, where Newtonian Noise could place a limit on

the interferometer's sensitivity and become the dominant noise source at lower frequencies [7].

### 1.3.3 Controls Noise

In order to hold the interferometer optics in resonance, a feedback system is utilized. The length control loops manage the optic's position while the angular control loops points the optics toward each other [6]. Electromagnetic coil actuators or electrostatic drives are able to hold the optics in place so that the control loops can suppress displacement noise such as seismic noise. Radio-frequency photodetectors (RFPDs) detect Pound-Drever-Hall (PDH) error signals which conveys information on where to hold the optics [6]. However, sensor noise such as shot noise, "dark" noise, and analog-to-digital noise are limitations on the RFPD and are difficult to distinguish from displacement noise. Therefore, LIGO controllers have been made to be strong during the locking phase to hold the optics and avoid displacement noise pollution, which does inject excess sensor noise, but at the end of the locking process, the hold is weakened to avoid sensor noise injection [6]. A feedforward system is utilized to counteract the sensor noise as the sensor noise is constantly being measured. Because controls noise dominates the GW spectrum at low frequencies, as shown in Figure 2, reducing or countering controls noise is a high priority [6]. Currently, there are works on more advanced feedforward systems, multiple-input multiple-output controls models, and better quantification of important parameters like optical losses and beam mode-matching to counteract controls noise.

### 1.3.4 Quantum Noise

Quantum noise arises due to the inherent nature of the uncertainty relation between phase and amplitude in light waves. Within a normal vacuum state, the total uncertainty, caused by the fluctuations in the electric and magnetic fields, is equally distributed between the phase and amplitude. These create what is known as "shot noise", caused by the fluctuating arrival times of photons, and "radiation pressure noise", which is the fluctuation on the mirror's positioning due to radiation pressure from photon flux [8]. By injecting phase squeezed light to turn a normal vacuum state into a squeezed vacuum state, the phase uncertainty can be lowered at the cost of increasing the amplitude uncertainty. This means a reduction in the shot noise is attained and an increase of at least the same amount of radiation pressure noise is added [1]. Phase squeezing was accomplished during the O3 run [9]. As of O4, LIGO can now target radiation pressure noise at low frequencies and shot noise at high frequencies due to the introduction of a 300 m filter cavity to the squeezing optics. This process is known as "frequency dependent squeezing" [9].

### 1.3.5 Thermal Noise

While increasing the power stored in the cavities increases the sensitivity of the interferometer, this comes with the consequences of radiation-pressure-induced angular instabilities, parametric instabilities, and thermo-optical distortion [10]. As a "Gaussian beam" is injected into the system, thermal defects "scatter" the laser light from the TEM00 mode, affecting the performance of the interferometer due to absorption of the incoming light.

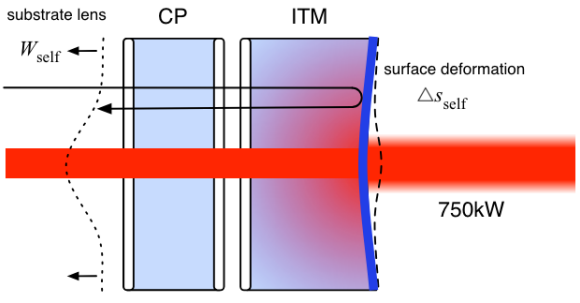


Figure 3: Illustration showcasing thermo-refractive substrate lens and thermo-elastic surface deformation, two sources of thermal distortion caused by self heating, originally from Ref. [7].

This creates temperature fluctuations within the coating and bulk substrate of the mirror resulting in a radial temperature gradient [10]. These temperature fluctuations lead to changes in the index of refraction of the substrate as well as surface deformations on the mirrors from thermal expansion. Such distortions cause the fields from the arms to no longer cancel out perfectly and thus degrades the interference pattern making low phase shifts from GWs more difficult to read [1].

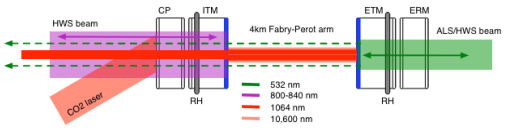


Figure 4: Diagram of the TCS from Ref. [7].

To minimize the thermal-induced spatial distortions created by the high power laser, the Thermal Compensation System (TCS), an adaptive optical system, was implemented [10]. The components that make up the TCS include ring heater actuators, spatially tunable $CO_2$ laser projectors, and Hartmann wavefront sensors which all work together to measure and compensate for distortions without introducing more noise. The Hartmann wavefront sensors (HWS) measure the thermal lensing in the mirrors while the ring heater (RH) actuators apply heating that induces a counter distortion of the mirrors. By using a $CO_2$ laser to heat the compensation plate (CP), a tunable thermal lens for the recycling cavities is additionally created [10].

## 1.4 FROSTI

One of the biggest limitations for future upgrades of LIGO and for Cosmic Explorer is test mass thermal defects due to increased arm cavity power. As higher power is being introduced in the interferometer, light absorption becomes more problematic. Point absorbers, perturbations on the mirror surface that arose during the fabrication process, additionally scatters the laser light and limits power buildup. The Front Surface Type Irradiator (FROSTI) ring heater seeks to counteract both of these issues.

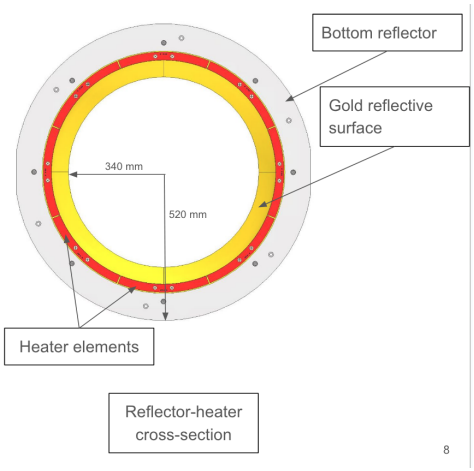


Figure 5: Diagram showcasing the anatomy of the FROSTI ring heater.

FROSTI is an annular ring heater that is 34 cm in diameter that will be placed 5 cm in front of the test masses [11]. The shape was selected based on the idea of nonimaging elliptical concentrators which seeks to optimize the radiative transfer from a source to a target. The reflector component of the ring heater is coated in thin gold film to maximize reflectivity. A corrective heating pattern is applied onto the highly reflective front surface of the test mass by FROSTI through eight infrared emitting heater elements composed of aluminum nitride.

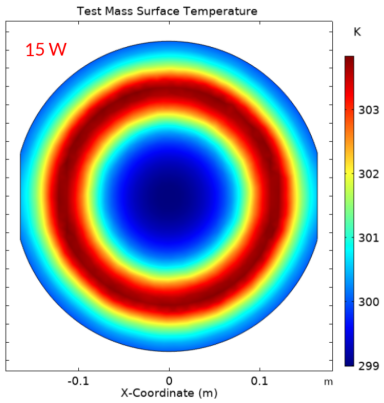


Figure 6: Example test mass temperature gradient from FROSTI profile.

The use of FROSTI alongside the current TCS could lead to improvements in arm power with lower SQZ loss as shown in Figure 7. Both in-air and in-vacuum tests have already been conducted for the FROSTI prototype to demonstrate its compatibility with the LIGO environment as well as to measure the thermal profile produced.

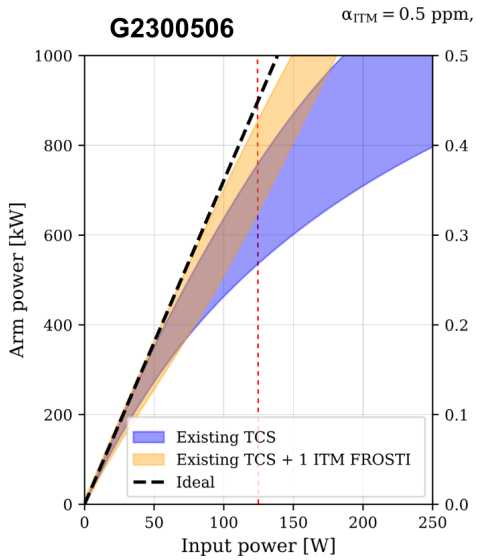


Figure 7: A comparison of the achievable arm power using just TCS (blue) to using TCS with FROSTI (yellow).

## 2 Objectives

As a demand for higher sensitivity persists for advanced LIGO, so too does a demand for higher arm cavity power. FROSTI aims to work with the existing TCS to compensate for the increase in optical losses from thermal distortions. While a prototype has been developed, further testing is needed to probe the feasibility of a multi-ring FROSTI by characterizing the profiles of the heater elements. Additionally, analysis and tuning of the heater elements may be made to probe the possibility of reducing losses caused by beam miscenterings. An optimal heating profile can then be selected that will account for losses from both thermal distortions and beam miscenterings to maximize optical gain. The overall goal is to quantify how much realistic beam miscenterings will degrade FROSTI's correction capability and how this can be mitigated by optimizing the power of each heater element.

## 3 Approach

The project is broken into two phases. The first few weeks of the program focused on the completion of the first phase which aimed to gather and analyze data of the heater elements from the prototype. The first week saw a complete clean sweep of the lab and the reinstallation of the FROSTI equipment. The setup utilized a blackbody screen to act as a substitute for the test mass as it re-emits the radiation incident on it and a FLIR A70 infrared camera to measure the thermal profiles produced with a 640 x 480 microbolometer array as shown in Figure 8. Data was collected through the camera using methods discussed in [12]. While the blackbody screen was already set up on the optical table in the clean room, the FROSTI and FLIR camera needed to be reinstalled after returning from in-vacuum testing at Caltech.

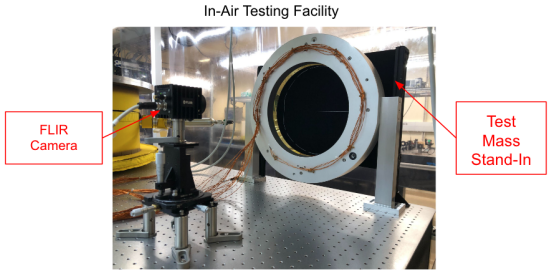


Figure 8: Testing setup of the Ring Heater, Test Mass substitute, and IR Camera.

After carefully transporting and setting up the FROSTI prototype, the power chassis to control individual heater elements was attached and powered on. It was discovered that one of the FROSTI DB-25 connector pins had snapped from the wire connected to it, causing no power to be sent to one of the elements. Once it was

re-crimped, all heater elements operated successfully, and the data collecting process could start. This required powering on only one element and measuring the resulting heater profile before turning it off and repeating for each of the other elements.

Figure 9: The chassis used to control the individual heater elements.

Each element was powered on with 24 V for approximately 45 minutes to allow for stabilization. The element was then turned off and left alone for 15 minutes before the next element was powered on. The element turned on next was chosen as the one furthest away to minimize any effects the previous element could have on the measured element's profile. After finishing the collection of the data in the laboratory, analysis was done using python to form a temperature profile for a singular average heater element.

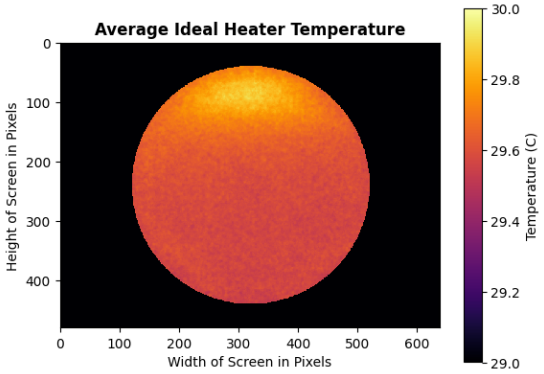


Figure 10: The average heating profile produced by an idealized heater element.

This was created by selecting one snapshot from each of the 8 individual elements gathered and rotating the data so that the heating profiles overlapped with each other. The average of all elements together was taken to form the average temperature profile of an ideal singular element. A circular mask was applied in preparation to export the data for COMSOL use later on.

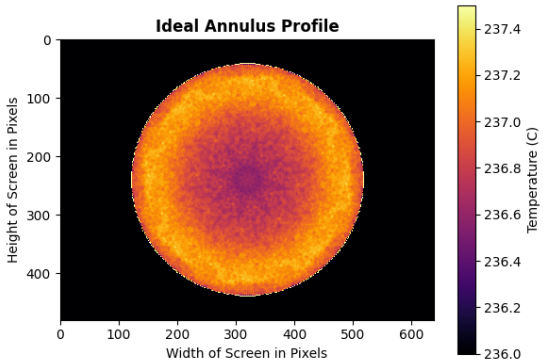


Figure 11: The heating annulus profile created from just copying, rotating, and adding the idealized heater element together (not averaged).

This idealized element was copied and rotated 7 times to produce an idealized heating profile pattern where all 8 "elements" are turned on.

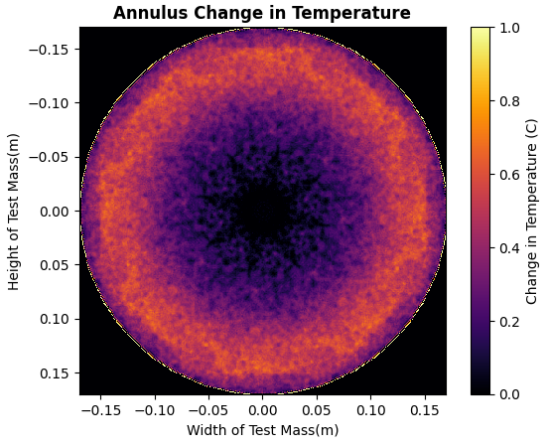


Figure 12: The change in temperature heating annulus profile from averaging and converted from pixels to meters.

Due to the way the elements were added together to produce the idealized heating profile pattern, to average out and get the actual change in temperature, an average temperature of a circular region of 10 pixels around the center was taken to act as the ambient temperature and subtracted from the overall profile to find the change

in temperature. The graph was subsequently cropped and converted from pixels to meters to better accurately model the profile onto a "test mass". To find the irradiance profile that generated this $\Delta$T profile, assumptions on how it looked needed to be made and testing those assumptions could be done through COMSOL. Thus a model of the blackbody screen and its properties was constructed in COMSOL with considerations of the convection through air as the measurements were done in-air rather than in-vacuum.

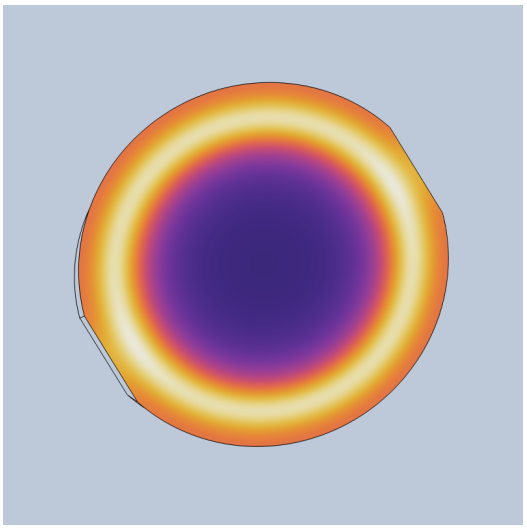

Figure 13: The resulting thermal profile on the "test mass" stand-in, generated in COMSOL from an input model irradiance that produced the best match to the measured temperature profile.

With the lack of information available on the thermal properties of the blackbody stand-in coating, the thermal properties of the aluminum substrate were used instead aside from the emissivity, which was kept at 0.99. Aluminum 6063 was chosen for the thermal conductivity while the heat transfer coefficient was chosen to be 17W/m$^2$·K based on the information from [13]. From the given range of 13-21 W/m$^2$·K, the model did not produce any noticeable changes in the outputs, thus 17W/m$^2$·K was sufficient.

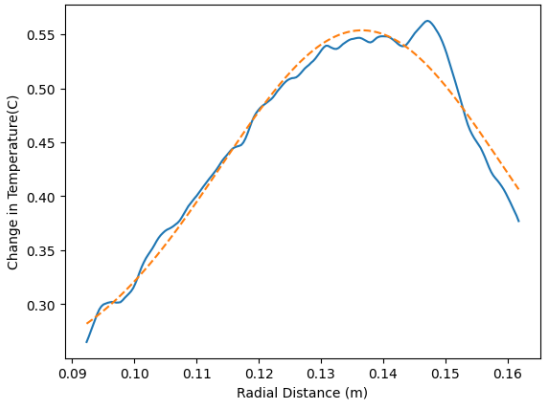


Figure 14: Gaussian fit on on side of a central slice of the measured temperature gradient profile.

To find the inferred irradiance from the measured temperature gradient profile, the location and width of the measured profile was needed. Analysis on the location and width of the temperature annulus was done by taking a vertical slice through the center and applying a gaussian fit.

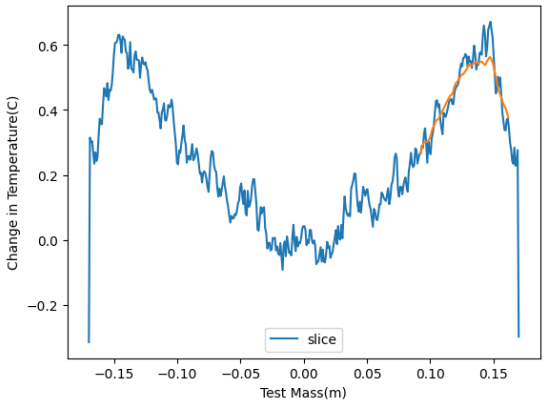


Figure 15: 1D plot of the central vertical slice of the measured temperature gradient profile with the gaussian curve fit overlayed.

The width of the in-air testing was roughly 0.0453m and located around 0.137m from the center. In comparison, when applying the same methods to the measured in-vaccum testing, that profile was roughly 0.041m in width and located only 0.119m from the center.

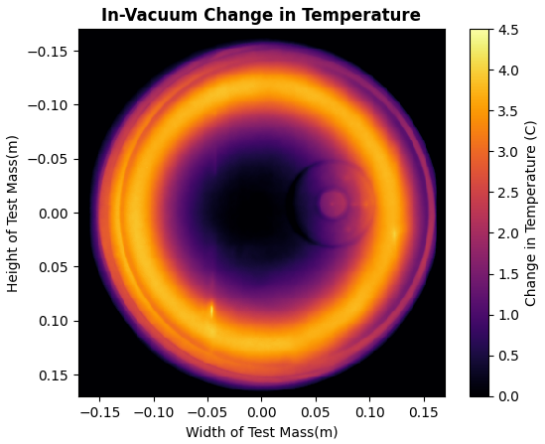


Figure 16: The in-vacuum heating profile.

This provided information on what a produced temperature profile from COMSOL should look like. To generate it, model irradiance profiles located in the same position as the measured in-air temperature were generated and fed into the model. The output change in temperature profile COMSOL produced were then compared to the measured profile. The input model irradiance profile that output the best matching temperature change profile was chosen to do a parametric sweep of the power in COMSOL. This provided a way to match the resulting range in the temperature gradient profile produced by COMSOL to the measured profile range.

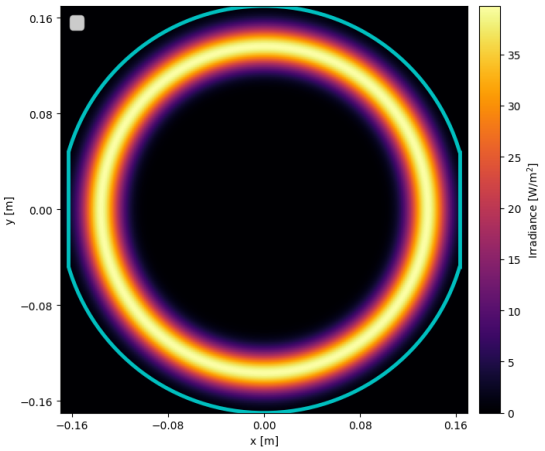


Figure 17: The generated fake irradiance profile that output the closest $\Delta$T profile to the measured idealized profile.

The closest change in temperature profile was produced by a generated irradiance profile with a width of roughly 0.0233m located at around 0.137m. The temperature gradient profile it produced in COMSOL had a width of roughly 0.0455m located at around 0.138m which can be explained from a slightly shifted gaussian fit than to the actual plot. Compared to the temperature change in-vacuum, the temperature change in-air is much lower due to loss from air convection and the heater elements not heating up to be as high as they could in-vacuum.

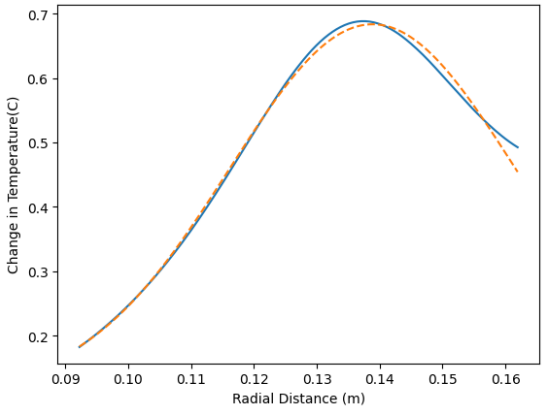


Figure 18: Gaussian fit on the change in temperature profile produced by most fitting generated irradiance profile input.

Having determined the location and estimated width that should be seen from both the irradiance and temperature profiles, COMSOL Ray Tracing can be utilized to create asymmetric irradiance profiles to apply to various static tilts of the test mass. Because the heating from FROSTI results in thermal expansion on the test mass, this could possibly be utilized to correct for minute misalignments of the test mass and reduce any resulting loss of sensitivity by applying an imbalanced heating profile.

## 4 Next Steps

Currently, an existing model of FROSTI in COMSOL needs to be edited such that the sin-

gular ring heater is cut into eight elements. Afterwards, this model can be used in COMSOL Ray Tracing to observe the behavior between the elements with non-uniform heating. The code used to generate irradiance profiles can then be updated to include this behavior and generate various asymmetric irradiance profiles. These will then be applied to a static tilt of the test mass to see which best minimizes the loss from misalignment. This will then be repeated for several different static tilts for robustness.

# 5 Timeline

| Period | Objective |
|---|---|
| Week 1 | Read papers to gain background information on Gravitational Waves and LIGO |
| Week 2 | Get familiarized with the laboratory facilities and clean room |
| Week 3 | Collect measurement data on irradiance profiles for each FROSTI element individually in the lab + rotationally align individual irradiance maps to produce an average temperature profile in Python |
| Week 4 | Visit Hanford LIGO site + become familiar with COMSOL + prepare first interim report |
| Week 5 | Build blackbody screen model in COMSOL + generate various fake irradiance profiles in Python |
| Week 6 | Determine location and width of irradiance annulus through comparison of fake irradiance profiles to measured temperature profile in COMSOL |
| Week 7 | Adjust FROSTI Ray Tracing Model in COMSOL to split heater ring into eight elements + prepare second interim report |
| Week 8 | Use COMSOL Ray Tracing to produce asymmetric irradiance profiles applied onto various static ”test mass” tilts |
| Week 9 | Analyze residual deformations from irradiance profiles on static tilts to find a relationship |
| Week 10 | Prepare final report and presentation |

## References


[1] Rana X Adhikari. Gravitational radiation detection with laser interferometry. 2013.

[2] The LIGO Scientific Collaboration. Advanced ligo. *Classical and Quantum Gravity*, 32(7):074001, mar 2015.

[3] Eanna E. Flanagan and Scott A. Hughes. The basics of gravitational wave theory. 2005.

[4] The LIGO Scientific Collaboration. Ligo: The laser interferometer gravitational-wave observatory. 2007.

[5] Muzammil A. Arain and Guido Mueller. Design of the advanced ligo recycling cavities.*Optics Express*, 16(14):10018, June 2008.

[6] Craig Cahillane and Georgia Mansell. Review of the advanced ligo gravitational wave observatories leading to observing run four. 2022.

[7] Lucia Trozzo and Francesca Badaracco. Seismic and newtonian noise in the gw detectors. *Galaxies*, 10(1):20, January 2022.

[8] J. Aasi, J. Abadie, and et. al. Enhanced sensitivity of the ligo gravitational wave detector by using squeezed states of light. *Nature Photonics*, 7(8):613–619, July 2013.

[9] L. McCuller, s. E. Dwyer, and et. al. LIGO's Quantum Response to Squeezed States. May 2021.

[10] Aidan F. Brooks, Benjamin Abbott, Muzammil A. Arain, Giacomo Ciani, Ayodele Cole, Greg Grabeel, Eric Gustafson, Chris Guido, Matthew Heintze, Alastair Heptonstall, Mindy Jacobson, Won Kim, Eleanor King, Alexander Lynch, Stephen O'Connor, David Ottaway, Ken Mailand, Guido Mueller, Jesper Munch, Virginio Sannibale, Zhenhua Shao, Michael Smith, Peter Veitch, Thomas Vo, Cheryl Vorvick, and Phil Willems. Overview of advanced ligo adaptive optics. 2016.

[11] Jonathan Richardson. Active Wavefront Control for Megawatt Arm Power. *LVK Meeting*. LIGO G2200399-v1, March 2022.

[12] Cassidy Nicks. Developing an in-air IR test facility for next-generation wavefront control. 2022.

[13] Khalifa, Abdul Jabbar mousawi, Israa. Comparison of Heat Transfer Coefficients in Free and Forced Convection using Circular Annular Finned Tubes. *ResearchGate* 5. 194-204. 2016.